



## ABSTRACT

5  
6 Extratropical regional-scale extreme precipitation events (EPEs) are usually associated with  
7 certain synoptic perturbations superimposed on slow-varying background circulations. These  
8 perturbations induce a dynamically forced ascent that destabilizes the atmospheric strati-  
9 fication and stimulates deep convection, which further drives the perturbation by releasing  
10 latent heat. This study identifies the characteristics of large-scale perturbations associated  
11 with summer EPEs in two representative regions, East China (ECN) and the southeastern  
12 United States (SUS), and analyzes the roles of dynamic forcings and diabatic heating using  
13 the quasi-geostrophic omega equation. Composites of 39 events in each region show that the  
14 upper-level absolute vorticity advection and tropospheric warm advection promote dynami-  
15 cally forced ascent in EPEs, and the moisture advection premoistens the local environment.  
16 The background circulation and synoptic perturbations in ECN and the SUS have signifi-  
17 cant differences. The background vorticity, temperature, and moisture advection form the  
18 quasi-steady Mei-Yu front in ECN, which provides favorable conditions for heavy rainfall. In  
19 the SUS, weaker background ascents are forced mainly through vorticity advection. In the  
20 synoptic scale, the EPEs in ECN are triggered by short-wavelength wave trains, and in the  
21 SUS, the EPEs are triggered by longer wavelength potential vorticity intrusions. Although  
22 the amplitudes of the dynamically forced ascent in the two regions are similar, diabatic heat-  
23 ing contributes much more to the vertical motion in ECN than the SUS, which indicates that  
24 there is stronger diabatic heating feedback there. The stronger diabatic heating feedback in  
25 ECN appears to be due to stronger moisture advection, convective environments with more  
26 humidity, and stronger coupling between convection and large-scale dynamics.

# 1. Introduction

Extreme precipitation events (EPEs) have great socioeconomic impacts, since they often lead to natural disasters such as floods, landslides, and urban waterlogging. However, the mechanism of EPEs is still poorly understood. Current global climate models (GCMs) face serious challenges in the simulation of precipitation extremes. For instance, many GCMs underestimate the climatology and interannual variations of precipitation extremes (e.g., *Kharin et al. 2007; Shiu et al. 2012*); and GCMs show a large inter-model spread of the future projection of precipitation extremes under global warming (*O’Gorman and Schneider 2009*). Examining the statistical characteristics of EPEs from observations is a useful starting point for developing a deeper understanding of EPEs. The observational characteristics of EPEs and its associated atmospheric circulation anomalies also could serve as benchmarks for improving GCM simulations and reducing their uncertainties.

There is an extensive literature on the atmospheric circulation anomalies associated with EPEs of different regions, and these studies showed that the EPE associated circulation anomalies have significant regional features. For example, the heavy rainfall leading to the devastating 2010 Pakistan flood is associated with a persistent upstream European block and monsoon depressions approaching from the tropics (*Houze et al. 1985; Lau and Kim 2012; Martius et al. 2013*). The heavy rainfall in central Europe is usually related to wave-breaking of a coherent wave-packet propagating from the central and eastern Pacific (*Martius et al. 2008; Wirth and Eichhorn 2014*). While a global survey is out the scope of this study, we focus on summer EPEs of two representative regions, East China (ECN) and the southeastern United States (SUS). One main regional feature of the summer EPEs of ECN is that they are usually embedded in the quasi-steady Mei-Yu front (e.g., *Yihui and Chan 2005; Luo et al. 2013*). The main factors affect the EPEs of ECN include upstream blocking highs (*Wang et al. 2000; Chen and Zhai 2014*), the western Pacific subtropical high (*Yihui and Chan 2005*), the South Asia high (*Wang et al. 2000*), the westerly jet (*Chiang et al. 2017*), and the moisture transport by low level southwesterlies (*Zhou and Yu 2005*). For the SUS region,

54 free tropospheric troughs (*Maddox et al.* 1979, 1980), surface frontal systems (*Funk* 1991),  
55 and low-level moisture and warm advection (*Konrad and Meentemeyer* 1994; *Konrad* 1997)  
56 are usually seen in EPEs. Many of the above studies are based on a single case and thus  
57 are unable to determine common features of EPEs. Moreover, since precipitation is directly  
58 related with vertical motion rather than horizontal winds, there is still a missing link when  
59 relating the atmospheric circulation anomalies to the EPEs.

60 Quasi-geostrophic omega ( $QG\omega$ ) analyses can serve as a useful tool to bridge the gap  
61 between large-scale circulation anomalies and local EPEs. The  $QG\omega$  equation has been used  
62 in the study of weather systems, such as the extratropical storms (e.g., *Clough et al.* 1996;  
63 *Lareau and Horel* 2011), Mei-Yu fronts (*Sampe and Xie* 2010; *Gu et al.* 2018), and EPEs  
64 (*Martius et al.* 2008), to quantify and separate vertical motion caused by perturbations at  
65 different levels or regions, taking the advantage of its linearity. However, most previous stud-  
66 ies of  $QG\omega$  analyses only focus on the dynamically forced vertical motion, those associated  
67 with the adiabatically-balanced flow. In the EPEs, there is a large amount of diabatic heat-  
68 ing due to the water vapor condensation, and the diabatic heating also induces significant  
69 large-scale vertical motion. Recent studies estimated that more than half of the large-scale  
70 vertical motion in EPEs are caused by diabatic heating (*Nie et al.* 2016; *Shaevitz et al.* 2016).

71 This study analyses the role of dynamic forcings and diabatic heating in extratropi-  
72 cal EPEs, and investigates their interactions. Large-scale adiabatic perturbations induce  
73 dynamically forced vertical motion and stimulate the development of deep convection by  
74 destabilizing the atmospheric stratification. The latent heat released by convection, in turn,  
75 drives further large-scale ascent by allowing air parcels to rise across surfaces of potential  
76 temperature. An extratropical EPE is essentially a large-scale-convection coupled system,  
77 in which the large-scale perturbations serve as forcings and the convective responses act as  
78 a feedback (*Nie and Sobel* 2016; *Nie et al.* 2018). We may call this view on EPEs as the  
79 “dynamic-forcing-adiabatic-feedback” perspective.

80 The goal of this paper is to identify the characteristics of large-scale conditions, including

81 both the background circulations and the synoptic-scale perturbations, as well as the dia-  
82 batic heating feedback associated with EPEs. We focus on the summer season EPEs in ECN  
83 and the SUS for a comparative study to identify their regional features. These two regions  
84 are local maximums of precipitation extremes (e.g., *van der Wiel et al. 2016; Sun and Zhang*  
85 *2017*), and their latitudes and Coriolis parameters are similar. The geographic locations of  
86 these two regions also share some similarity; they are both roughly located in the south-  
87 eastern corner of their respective continents and the entrance of the Northern hemispheric  
88 storm tracks. Section 2 introduces the data and methods. Section 3 examines the time  
89 evolution of the large-scale advective forcings associated with EPEs, followed by analyses of  
90 the horizontal meteorological fields in section 4. In section 5, we examine the dynamically  
91 forced and diabatic heating forced vertical motion components and investigate the causes  
92 for differences in the strength of the diabatic heating feedback in these two regions. Section  
93 6 includes the conclusions and discussion.

## 94 **2. Data and Methods**

95 This study mainly uses the ERA-Interim reanalysis dataset (*Dee et al. 2011*). The me-  
96 teorological variables in the ERA reanalysis have a 6-hour temporal resolution and a spatial  
97 resolution of  $0.7^\circ$ . The precipitation variable used here is the short-range ECMWF forecast,  
98 which is available at a 12-hour temporal resolution. The date range for all the data is from  
99 1979 to 2017.

100 The ECN region is defined as  $112^\circ E \sim 122^\circ E$ , and  $25^\circ N \sim 35^\circ N$  and the SUS region  
101 is defined as  $95^\circ W \sim 85^\circ W$  and  $28^\circ N \sim 38^\circ N$ . Thus, the EPEs in this study are regional-  
102 scales events, in contrast to convective-scale precipitation extremes. Our analyses focus on  
103 the summer season (June to August). An EPE is defined as a day with the daily maximum  
104 precipitation averaged over each regional box during each summer season. We exclude  
105 EPEs caused by tropical cyclones (including two events in ECN and seven events in the

106 SUS) since they have very different characteristics from those associated with extratropical  
 107 perturbations. From 1979 to 2017, 39 EPEs in each region are identified with a regional-box-  
 108 averaged mean precipitation of 17.5 *mm/day* in ECN and 11.7 *mm/day* in the SUS (table  
 109 1). These events are used for composites to remove random noises in individual events and  
 110 to obtain robust characteristics of EPEs.

111 The QG $\omega$  equation is a useful framework for understanding and quantifying the factors  
 112 associated with vertical motion in EPEs (e.g., *Martius et al.* 2013; *Nie et al.* 2016). The  
 113 QG $\omega$  equation may be written as (e.g., *Holton* 2004)

$$114 \quad (\partial_{pp} + \frac{\sigma}{f_0^2} \nabla^2) \omega = -\frac{1}{f_0} \partial_p Adv_\zeta - \frac{R}{p} \left(\frac{1}{f_0^2}\right) \nabla^2 Adv_T - \frac{R}{p} \left(\frac{1}{f_0^2}\right) \nabla^2 Q, \quad (1)$$

115 where  $\sigma = -\frac{RT}{p} \partial_p \ln \theta$  is the dry static stability,  $\omega$  is the pressure vertical velocity, and  $Q$  is  
 116 diabatic heating.  $\zeta = \frac{1}{f_0} \nabla^2 \phi + f$  is the geostrophic absolute vorticity,  $\phi$  is the geopotential,  
 117 and  $f_0$  is the reference value for the Coriolis parameter.  $Adv_\zeta$ ,  $Adv_T$  and  $Adv_q$  are the  
 118 horizontal advection of absolute vorticity ( $\zeta$ ), temperature ( $T$ ) and specific humidity ( $q$ ),  
 119 respectively. The QG $\omega$  equation states that to maintain the QG balance, vertical motion will  
 120 be induced by ageostrophic adjustments whenever there is horizontal advection of absolute  
 121 vorticity or temperature, or diabatic heating.

122 The total  $\omega$  may be separated into a component explained by the QG $\omega$  equation ( $\omega_{qg}$ )  
 123 and the remainder (named  $\omega_{aqq}$ , which is the a-QG component of  $\omega$ ).  $\omega_{qg}$  represents the  
 124 vertical motion due to the flow and heating with a length scale greater than the local Rossby  
 125 radius of deformation, and  $\omega_{aqq}$  includes contributions from higher-order (2nd order and  
 126 above) Rossby number terms and the effects from meso- and smaller scale systems that  
 127 are not captured in the QG dynamics. A significant advantage of the QG $\omega$  equation is its  
 128 linearity, and thus, we may directly decompose  $\omega_{qg}$  into components forced by the large-scale  
 129 advective forcings and diabatic heating. Therefore, we have

$$130 \quad \omega = \omega_{qg} + \omega_{aqq} = \omega_\zeta + \omega_T + \omega_Q + \omega_{aqq}. \quad (2)$$

131  $\omega_\zeta$ ,  $\omega_T$ , and  $\omega_Q$ , are the vertical motion components corresponding to  $Adv_\zeta$ ,  $Adv_T$ , and  $Q$

132 term, respectively, and their sum is  $\omega_{qg}$ . These terms are calculated by solving the QG $\omega$   
 133 equation (Eq. 1) on 3-dimensional sphere grids, including the right-hand-side (RHS) terms  
 134 one by one (*Stone* 1968; *Martius et al.* 2013; *Nie et al.* 2016). In solving Eq. 1, the upper  
 135 boundary condition is  $\omega = 0$  at a nominal tropopause of 100 *hPa*, and the lower boundary  
 136 condition is setting  $\omega$  to be its surface value at the surface level. The surfaces of the two  
 137 regions are relatively flat, and the orography forced  $\omega$  is very small; thus, it is not shown in  
 138 the following analyses. Since the first two RHS terms of Eq. 1 represent the dynamic forcing  
 139 of the adiabatic-balanced flow, the sum of  $\omega_\zeta$  and  $\omega_T$  may be called the dynamically forced  
 140 vertical motion ( $\omega_D$ ), in contrast to the diabatic heating component of vertical motion ( $\omega_Q$ ).  
 141  $\omega_{agg}$  is calculated as a residual term in Eq. 2. As shown later, for regional-scale EPEs,  $\omega_{qg}$   
 142 accounts for most of the total  $\omega$  in the regions of events, which validates our uses of the  
 143 QG $\omega$  in understanding EPEs.

### 144 3. Dynamic Forcings

145 In this section, we examine the EPE-associated dynamic forcings. Fig. 1 shows the  
 146 time evolution of  $Adv_\zeta$ ,  $Adv_T$ , and  $Adv_q$  averaged over each regional box. Day 0 denotes  
 147 the day with peak precipitation, while the negative (positive) sign denotes the days prior  
 148 (after). Although  $Adv_q$  does not directly force vertical motion, it modifies the local convective  
 149 conditions and thus affects the convective responses to the large-scale perturbations (*Nie et*  
 150 *al.* 2016). First, let us focus on the results for ECN. Over the 2 weeks around the EPEs,  
 151 there is a background  $Adv_\zeta$  that is negative in the lower to middle troposphere (900 *hPa*  
 152 to 400 *hPa*) and positive in the upper troposphere (400 *hPa* to 100 *hPa*) (Fig. 1a). The  
 153 synoptic-scale  $Adv_\zeta$  is superimposed on the background. From day -2 to day 0, the synoptic-  
 154 scale  $Adv_\zeta$  is positive throughout the troposphere with a maximum value in the upper  
 155 troposphere, followed by negative  $Adv_\zeta$  at day +1. The background  $Adv_T$  is negative in the  
 156 planetary boundary layer (PBL) and positive near the tropopause (Fig. 1c). There is also a

157 warm background  $Adv_T$  extending throughout the troposphere (seen later in Fig. 2d). The  
 158 synoptic scale  $Adv_T$  is positive throughout the troposphere preceding day 0; then, it becomes  
 159 negative after day 0. The background  $Adv_q$  is positive with a peak in the PBL and decreases  
 160 upward since most atmospheric moisture is confined to the low levels. In the synoptic scale,  
 161 there is a strong positive anomaly of  $Adv_q$  extending from the surface to 400  $hPa$  from day  
 162 -2 to day 0, which is followed again by negative anomalies. The negative  $Adv_q$  after day 0  
 163 (although the moisture flux convergence is still positive) is because the heavy rainfall makes  
 164 the region as moist as or even moister than the equatorward regions upwind.

165 In the SUS, the background  $Adv_\zeta$  in the upper troposphere is positive but relatively weak,  
 166 and the negative values are close to the surface (Fig. 1b). In the synoptic scale, there is  
 167 also a robust positive  $Adv_\zeta$  in the upper troposphere; however,  $Adv_\zeta$  is negative in the lower  
 168 troposphere. The background  $Adv_T$  is both positive in the PBL and near the tropopause  
 169 (Fig. 1d). For background moisture advection, there is a weak positive  $Adv_q$  in the PBL,  
 170 while the levels above are negative with the peak occurring at about 850  $hPa$  (Fig. 1f).  
 171 The synoptic scale  $Adv_T$  and  $Adv_q$  in the SUS show similar signals to those in ECN, with a  
 172 positive anomaly before day 0 and negative anomalies after day 0, except these signals are  
 173 much weaker.

174 The large-scale advective terms in Fig. 1 show mixed signals of the background circula-  
 175 tions and synoptic perturbations. The background signals represent the contribution of the  
 176 slow-varying general circulation, while the synoptic-scale signals represent the fast-varying  
 177 perturbations that directly trigger EPEs. To separate these signals, we decompose each  
 178 meteorological variable into a background component (means from day -13 to day -4 and  
 179 day +4 to day +13) and a synoptic-scale component (the differences between the total and  
 180 the background component). For example, with temperature, we have  $T = \bar{T} + T'$ , where  
 181  $\bar{T}$  and  $T'$  denote the background and synoptic-scale component, respectively. Thus, the  
 182 temperature advection may be decomposed into four parts,

$$183 \quad Adv_T = -\mathbf{V} \cdot \nabla T = -\bar{\mathbf{V}} \cdot \nabla \bar{T} - \bar{\mathbf{V}} \cdot \nabla T' - \mathbf{V}' \cdot \nabla \bar{T} - \mathbf{V}' \cdot \nabla T'. \quad (3)$$

184 The RHS terms in Eq. 3 are the background advection (RHS-1, background temperature  
 185 advection by background winds), the cross terms (RHS-2 and RHS-3), and the nonlinear  
 186 advection (RHS-4, perturbation temperature advection by perturbation winds), respectively.  
 187 The decomposition is not sensitive to the choice of averaging days; varying the criterion for  
 188 the decomposition within several days leads to very similar results.

189 The decompositions of the advective terms based on Eq. 3 clearly separate the synoptic  
 190 scale advection (the cross terms and the nonlinear term in Eq. 3) from its background,  
 191 allowing us to identify their contributions and to compare their differences in the two regions  
 192 separately. We first observe that every term in Eq. 3 has a nonnegligible contribution to the  
 193 total advection. In the ECN, the background advective terms (Fig. 2a,d,g) show consistent  
 194 but cleaner results compared with those described in Fig. 1. By examining the cross terms,  
 195 we found that the RHS-2 term has similar patterns to the RHS-3 term but has the opposite  
 196 sign and a larger amplitude (figures omitted). Thus, we only show the sum of the cross  
 197 terms in Fig. 2-3 (middle columns). By comparing Fig. 2 with Fig. 1, we see that the  
 198 cross terms contribute to most of the synoptic-scale signals in total advection, including the  
 199 upper level positive  $Adv_\zeta$  (Fig. 2b), the positive then negative  $Adv_T$  (Fig. 2e) and  $Adv_q$   
 200 (Fig. 2h) around day 0. For EPEs, the nonlinear term contributes to the positive  $Adv_\zeta$  near  
 201 the surface, which dominates the negative  $Adv_\zeta$  in the cross terms. Other than that result,  
 202 the nonlinear term has a small contribution to the synoptic-scale signals. In contrast, the  
 203 nonlinear term has sizeable projections for the background scale (i.e.,  $-\overline{\mathbf{V}' \cdot \nabla T'}$  taking  $T$   
 204 as example) due to the daily synoptic waves (which are not the ones associated with EPEs)  
 205 in the ECN regions.

206 The decompositions of the advective terms in the SUS (Fig. 3) show generally weaker  
 207 signals than those in ECN, with some differences. Again, the background advective terms  
 208 confirm our previous observation. Compared to the results in ECN, there is no warm back-  
 209 ground advection in the free troposphere, except near the tropopause (Fig. 3d). The back-  
 210 ground moisture advection has positive peaks in a thin layer near the surface and is negative

211 above (Fig. 3g). The cross terms also largely contribute to the synoptic-scale signals in  
 212 total advection. Unlike in ECN, where the cross terms show signals with changed signs from  
 213 day -2 to day 2, in the SUS, the cross terms show single peak signals around day 0. The  
 214 nonlinear advection in the SUS plays a larger role in EPEs than it does in ECN.

215 The advection of vorticity and temperature can dynamically force large-scale vertical  
 216 motion that further causes heavy rainfall. The time evolution of the  $\omega$  components corre-  
 217 sponding to the dynamic forcings are shown in Fig. 4a-d. The QG $\omega$  equation states that  
 218 upward gradients of  $Adv_\zeta$  (e.g., positive on upper levels and negative on lower levels) and  
 219 positive  $Adv_T$  induce ascent, while the downward gradient of  $Adv_\zeta$  and negative  $Adv_T$  induce  
 220 descent. Consistent with these qualitative arguments, there is free tropospheric background  
 221 ascent in  $\omega_\zeta$  and  $\omega_T$  in ECN (Fig. 4a,c) that corresponds to the background  $Adv_\zeta$  (Fig. 2a)  
 222 and  $Adv_T$  (Fig. 2d). The importance of the background warm advection in the maintenance  
 223 of the Mei-Yu front in East Asia has been pointed out in previous studies (*Sampe and Xie*  
 224 2010). Here, we show that the background  $Adv_\zeta$  is at least equally important. Before the  
 225 ECN EPEs (day -2), there is actually weak descent in  $\omega_\zeta$  (Fig. 4a), which corresponds to  
 226 the upper tropospheric negative  $Adv_\zeta$  in Fig. 1a. At day 0 to day +1, the strong positive  
 227  $Adv_\zeta$  in the upper troposphere forces strong upward  $\omega_\zeta$ . The upward  $\omega_T$  peaks at day -1  
 228 followed by descent at day +1 (Fig. 2c), which is consistent with the pair of positive and  
 229 negative  $Adv_T$  values there. In the SUS, the background  $\omega_\zeta$  is more bottom heavy than it is  
 230 in ECN, which is consistent with the less tilted structure of  $Adv_\zeta$  (Fig. 3a). The background  
 231  $\omega_T$  for the SUS is very weak. In the synoptic scale,  $\omega_\zeta$  shows a single strong ascent over the  
 232 EPE period. There is also an ascent in  $\omega_T$  at day -1; however, the descent after day 0 is  
 233 very weak. In the SUS,  $\omega_\zeta$  is greater than  $\omega_T$ , which indicates that there is a relatively more  
 234 important role for  $Adv_\zeta$  there; by contrast, in ECN,  $Adv_\zeta$  and  $Adv_T$  have similar importance  
 235 in forcing EPEs.

## 4. Horizontal Patterns

To better understand the large-scale advective terms seen in the previous section, we examine the horizontal patterns of the background and synoptic components of meteorological variables. We first look at the background geopotential ( $\bar{\phi}$ ) and horizontal winds ( $\bar{\mathbf{V}}$ ) in Fig. 5. On 850 *hPa* (Fig. 5a), ECN is located at the west edge of the Pacific subtropical high. The pressure gradient between the Pacific subtropical high and the low-pressure regions to its west induces prevailing southwesterlies. The southwesterlies bring air with low planetary vorticity, warm temperature, and moisture from the tropics (which is consistent with the lower-level negative  $Adv_{\zeta}$  in Fig. 2a, positive  $Adv_T$  in Fig. 2d, and positive  $Adv_q$  in Fig. 2g). At 200 *hPa* (Fig. 5e), the Pacific subtropical high disappears, while the South Asia high shows dominant influences (e.g., *Rodwell and Hoskins* 2001; *Nie et al.* 2010). The anticyclonic winds of the South Asia high bring northerlies over ECN, which is consistent with the upper-level positive  $Adv_{\zeta}$  in Fig. 2a. The northern part of the ECN regional box is covered by the middle-latitude westerly jet, which brings warm air from the South Asia high to ECN (thus the upper-level positive  $Adv_T$  in Fig. 2d). At 500 *hPa* (Fig. 5c), the geopotential field is dominated by the Pacific subtropical high, and southwesterlies are formed over ECN due to the Pacific subtropical high and the westerly jet.

Moving to the SUS region, at low levels, the Atlantic subtropical high induces southeasterlies (Fig. 5b), which leads to the negative  $Adv_{\zeta}$  shown in Fig. 3a. At 200 *hPa* (Fig. 5f), which is similar to the case for ECN, there is a low-latitude high-pressure system to the southwest of the SUS regional box. Together with the westerly jet, the northwesterlies provide strong upper-level positive  $Adv_{\zeta}$  and  $Adv_T$  (Fig. 3a,d). At the middle tropospheric levels (Fig. 5d), the geopotential field is influenced by both the downward extension of the upper-level low-latitude high pressure and the upward extension of the Atlantic subtropical high. Moreover, there is a high-pressure ridge over the Rocky Mountains, which is presumably caused by topographic effects. The high-pressure ridge induces southward meridional winds in the SUS, in contrast to the northward meridional winds in ECN. The differences in

263 the middle troposphere explain why the background  $Adv_\zeta$  and  $\omega_\zeta$  in ECN are more top-heavy  
264 than those in the SUS.

265 For the background moisture advection, one may examine the precipitable water super-  
266 imposed on the low-level winds only, since moisture concentrates at the levels close to the  
267 surface. The low-level southwesterlies transport moisture from the West Pacific warm pool  
268 and the South China Sea, which are regions with abundant moisture, to ECN (Fig. 5g), and  
269 this result is consistent with the strong positive  $Adv_q$  in Fig. 2g. In contrast, the moisture  
270 gradient in the SUS is weak (Fig. 5h). The Caribbean Sea region, despite its high sea surface  
271 temperature, is relatively dry due to the strong free tropospheric subsidence associated with  
272 the Atlantic subtropical high (*Peixoto and Oort* 1992). Since there is no deep convection  
273 to transport moisture to the upper levels, moisture is confined to the surface layer, and the  
274 humidity in the free troposphere is very low. As a result, in the SUS,  $Adv_q$  is only positive  
275 in the PBL and is negative above it (Fig. 3g). The total background moisture advection in  
276 the SUS is much weaker than that in ECN.

277 Although the background states (Fig. 5) are close to the summer season mean, there are  
278 sizable differences between them, which are largely due to the intra-seasonal variations. At  
279 850  $hPa$ , the background in ECN shows that the Pacific subtropical high extends southwest-  
280 ward, leading to anomalous southerlies (Fig. 6a). At the middle and upper levels, a south-  
281 ward shift of the westerly jet favors the EPEs in ECN (Fig. 6c,e). The jet shift moves the jet  
282 entrance further south, inducing additional upper-level divergence and thus upward vertical  
283 motion in the southwest quadrant of the jet streaks (where the ECN region is) (*Uccellini and*  
284 *Kocin* 1987; *Chen and Zhai* 2014; *Chiang et al.* 2017). The southwestward extension of the  
285 Pacific subtropical high and the southward shift of the jet also bring anomalous moisture  
286 flux transport to ECN (*Zhou and Yu* 2005), which corresponds to a southward shift of the  
287 Mei-Yu front. In the SUS, the background state also reveals a westward strengthening of the  
288 Atlantic subtropical high and associated southerly anomalies (Fig. 6b). Additionally, to the  
289 north of the SUS, there are several low-pressure centers throughout the troposphere, which

290 seems to be a planetary-scale Rossby wave train that propagates from the Pacific to Canada.  
291 The precipitable water anomalies (Fig. 6g,h) are roughly consistent with the geopotential  
292 anomalies. The extended subtropical high leads to negative anomalies due to subsidence.  
293 The south shift of the jet corresponds to the south shift of the Mei-Yu front, and thus, there  
294 are dry anomalies to the north of the ECN regional box. One might expect that there are  
295 moist anomalies in the regional boxes in the background state; however, this outcome was  
296 not observed in our analysis.

297 Next, we examine the synoptic-scale components of the meteorological variables in Fig.  
298 7. We only show results at 200 *hPa* where the upstream influences of the synoptic-scale  
299 signals are most obvious. In the lower-to-middle troposphere, a cyclonic low-pressure center,  
300 which is tilted westward with height, develops in both regions (figure omitted). In ECN, the  
301 EPEs are associated with a wave train that propagates over the northern part of the regional  
302 box (Fig. 7a-c). The wavelength of the wave train is relatively short ( $\sim 3500$  *km*), and the  
303 propagation speed is fast; from day -1 to day +1, the positive center has moved from the  
304 northwest corner of the regional box to about 15 degrees east. The EPE-associated synoptic-  
305 scale perturbations in the SUS are quite different (Fig. 7d-f). A slow-moving, large-scale  
306 wave train (with a wavelength of  $\sim 8000$  *km*) propagates from the North Pacific to the north  
307 of the SUS. The influence of the large-scale wave train on a heavy rainfall is a common feature  
308 in many regions; for example, the heavy rainfall in South Brazil is associated with the Pacific  
309 South America Pattern (*Cavalcanti* 2012; *Mo and Higgins* 1998). The strong low-pressure  
310 center over Northeast Canada develops a tail that extends to the west of the SUS. The  
311 secondary low-pressure center slowly intrudes into the SUS and detaches from the parent  
312 wave train. At day +1, a new positive geopotential center develops to the east of the SUS due  
313 to the diabatic heating of the heavy precipitation. This type of synoptical situation is usually  
314 called a potential vorticity (PV) intrusion (*Massacand et al.* 1998; *Waugh and Polvani* 2000;  
315 *Funatsu and Waugh* 2008). The differences in the synoptic-scale perturbations in ECN and  
316 the SUS are expressed in the advective terms in Fig. 2-3. The fast propagating wave train

317 in ECN leads to changes in signs of the cross term in advection (Fig. 2b,e), whereas the PV  
318 intrusion in the SUS is a slow process, so the cross term in advection shows only a single  
319 peak in the signal (Fig. 3b,e).

## 320 5. Diabatic Heating Feedback

321 In previous sections, we examined the dynamic forcings associated with the adiabatic flow  
322 in EPEs and the horizontal patterns to understand the forcings. In this section, we focus  
323 on diabatic heating feedback on vertical motion. The questions to be addressed include  
324 determining how large the contribution of diabatic heating to  $\omega$  is and what causes the  
325 differences in diabatic heating feedback in the two regions.

326 The time evolution of the diabatic heating component of  $\omega$  ( $\omega_Q$ ) and the total  $\omega$  are shown  
327 in Fig. 4e-h. We first observe that there is an obvious diurnal cycle of  $\omega$  corresponding to  
328 the diurnal cycle of convection. In both regions,  $\omega_Q$  has the largest contribution to total  $\omega$   
329 among the four components in Eq. 2. In ECN, there are two peaks of  $\omega_Q$  during the EPEs,  
330 which correspond to the peak of  $\omega_T$  and peak of  $\omega_\zeta$  (Fig. 4a,c), respectively. The first peak  
331 is more top-heavy than the second. In the SUS, there is only one peak of  $\omega_Q$  at day 0, which  
332 is mainly forced by  $\omega_\zeta$  (Fig. 4b). Comparing  $\omega_Q$  in both regions shows that  $\omega_Q$  in ECN is  
333 much greater than that in the SUS.

334 Next, we examine the horizontal distributions of  $\omega$  and its components at 500 *hPa* (Fig.  
335 8). As expected, regions with heavy rainfall (white contours in Fig. 8) collocate with centers  
336 of strong ascent. In ECN, one can see the background Mei-Yu front extending from Indochina  
337 to Japan (Fig. 8a).  $\omega_D$  in ECN shows alternating ascent and descent centers extending from  
338 the upstream to the regional box, which is consistent with the synoptical perturbation of the  
339 upper tropospheric wave train (Fig. 8c; note that the domain in Fig. 8 is smaller than the  
340 domain of previous figures).  $\omega_D$  also has a sizeable projection for the background Mei-Yu  
341 front, which confirms previous studies showing the important dynamic forcings on the Mei-

342 Yu front (e.g., *Sampe and Xie* 2010; *Gu et al.* 2018). There is only one ascent center of  $\omega_D$   
 343 over the SUS, corresponding to the PV intrusion process.  $\omega_Q$  in both regions has a smaller  
 344 spatial scale than  $\omega_D$  and is concentrated in the regional boxes. It is interesting to note that  
 345 in both regions, the centers of  $\omega_D$  are several degrees north of the centers of  $\omega_Q$ , presumably  
 346 because the environment is moister in the south and the moisture is transported from the  
 347 south. When the moist air meets dynamically forced ascent of only sufficient strength, not  
 348 necessarily the peaks of ascent, strong convection develops. We also observe that although  $\omega_D$   
 349 has similar amplitude in these two regions,  $\omega_Q$  in ECN is much greater than that in the SUS.  
 350 The a-QG component  $\omega_{agg}$  is small in the regional boxes, confirming our start point that the  
 351 QG  $\omega$  is a good approximation of total  $\omega$  in extratropical EPEs. The fact that  $\omega_{agg}$  in ECN  
 352 is larger than that in the SUS suggests larger roles for subscale (mesoscale and convective  
 353 scale) disturbances in contributing large-scale vertical motion.  $\omega_{agg}$  is particularly large in  
 354 the tropical rain-belt south of the regional boxes because when moving towards tropics, the  
 355 Rossby radius of deformation approaches infinity, and perturbations of most length scale  
 356 become the “small scale” perturbations that are not captured by QG theory.

357 The vertical profiles of  $\omega$  and its components averaged over the two regions at day 0 are  
 358 shown in Fig. 9.  $\omega_D$  in the two regions has similar amplitudes, although  $\omega_D$  in the SUS  
 359 is more bottom heavy than that in ECN. It is the difference in  $\omega_Q$  in the two regions that  
 360 make the total  $\omega$  in ECN much greater than  $\omega$  in the SUS, which is consistent with the  
 361 intensity of EPEs in the two regions (table 1). To better quantify the relative importance of  
 362  $\omega$  components, one may convert  $\omega$  to precipitation with a scaling proposed by *O’Gorman and*  
 363 *Schneider* (2009) in which  $P \approx -\frac{1}{g} \int \omega \partial_p^* q|_{\theta_e^*} dp$ . This scaling is the vertical integration of  $\omega$   
 364 times the vertical gradient of saturation-specific humidity following a moist adiabatic process  
 365 ( $\partial_p^* q|_{\theta_e^*}$ ). Precipitation approximated by total  $\omega$  with this scaling is very close to the same  
 366 value in the reanalysis (table 1). Similarly, we can calculate the approximate precipitation  
 367 corresponding to each component of  $\omega$  (table 1). Precipitation corresponding to  $\omega_D$  ( $P_D$ )  
 368 in the two regions has a similar value; however, precipitation corresponding to  $\omega_Q$  ( $P_Q$ )

369 in ECN is much greater than that in the SUS. One may define a diabatic heating feedback  
370 parameter ( $\alpha$ ) as the ratio between  $P_Q$  and  $P_D$  (Nie *et al.* 2018). The  $\alpha$  parameter quantifies  
371 the diabatic heating feedback on precipitation due to QG adjustments, given a normalized  
372 unit of adiabatic large-scale perturbations. The  $\alpha$  values in ECN and the SUS are 2.1 and  
373 1.1 (the value of  $\alpha$  in the SUS is similar to a case study of Texas extreme precipitation in  
374 2015 (Nie *et al.* 2018)), respectively, indicating that there is much stronger diabatic heating  
375 feedback in ECN.

376 Here, we provide qualitative reasoning on the causes of the differences of  $\alpha$  in the two  
377 regions. Due to the complexities in convection, quantitative analyses usually require help  
378 from numerical simulations. The diabatic heating feedback represents how local convection  
379 responds to large-scale perturbations in the coupled system, and thus, it may mainly depend  
380 on the following factors (Nie and Sobel 2016): 1. the large-scale forcings, i.e., the combination  
381 of  $Adv_C$ ,  $Adv_T$ , and  $Adv_q$ ; 2. the local convective environments, i.e., the temperature and  
382 moisture profiles; and 3. the characteristic wavelength of the system, which determines how  
383 strongly convection and large-scale dynamics are coupled (Nie and Sobel 2016; Tandon *et*  
384 *al.* 2018a,b). Next, we examine these factors in the two regions to understand how they  
385 contribute to the differences of  $\alpha$ .

386 First, the large-scale forcings favor larger  $\alpha$  in ECN due to the stronger  $Adv_q$  preceding  
387 the EPEs. Positive  $Adv_q$  moistens the local environments and strengthens the convective  
388 responses. The modification can be quite large (Nie *et al.* 2016) since convection sensitively  
389 depends on environmental moisture (e.g., Derbyshire *et al.* 2004). For dynamic forcings,  $\omega_D$   
390 in the SUS is more bottom heavy than in ECN. In addition,  $\omega_T$  has more contributions to  $\omega_D$   
391 in ECN than in the SUS. Although warm advection forces ascent dynamically, it inhibits the  
392 development of convection by increasing atmospheric stability. These two factors favor larger  
393  $\alpha$  in the SUS; however, these effects are minor and should be dominated by the modification  
394 of  $Adv_q$ .

395 Second, the local convective environments favor stronger diabatic heating feedback in

396 ECN. The  $T$  profile in ECN is approximately 1  $K$  warmer than the profile in the SUS  
397 (Fig. 10a), and the dry static stabilities in the two regions are similar (Fig. 10c). The  $q$   
398 profile in ECN is significantly larger than the profile for the SUS (Fig. 10b), which is partly  
399 due to the warmer temperature and partly due to the higher relative humidity (Fig. 10d).  
400 The precipitable water at day 0 is 47.4  $mm/day$  in ECN and 40.9  $mm/day$  in the SUS.  
401 Numerical simulations showed that diabatic heating feedback is strongly proportional to the  
402 atmospheric moisture (Nie *et al.* 2016, 2018) because increased moisture leads to increased  
403 diabatic heating, which further drives a dynamic increase in large-scale ascent (and thus  
404 larger  $\alpha$ ).

405 Finally, the characteristic wavelength of synoptic perturbations associated with EPEs in  
406 the ECN is only approximately half of the wavelength in the SUS (Fig. 7). The shorter the  
407 characteristic wavelength (i.e., the smaller the ratio between the characteristic wavelength  
408 and the Rossby radius of deformation), the stronger the large-scale dynamics and the convec-  
409 tion are coupled. A study using an idealized convection-large-scale coupled system supports  
410 the relationship between the wavelength and  $\alpha$  (Nie and Sobel 2016). Thus, compared with  
411 the PV intrusion in the SUS, the short-wavelength wave train in ECN also leads to stronger  
412 diabatic heating feedback there.

## 413 6. Conclusions and Discussion

414 Extratropical EPEs are usually associated with large-scale disturbances, strong upward  
415 motions, and large latent heat release, all of which are closely coupled together. Since the  
416 synoptic-scale perturbations are strongly constrained by the QG dynamics in the extratrop-  
417 ics, we develop herein a deeper understanding of EPEs from the perspective of the  $QG\omega$   
418 equation. We examine the dynamic forcings and convective feedbacks associated with sum-  
419 mer EPEs in two representative regions, East China and the southeastern United States,  
420 and compare their regional characteristics. The main findings are the following (see also the

421 schematic in Fig. 11 with minor points):

422 (1) EPEs in ECN and the SUS are associated with robust large-scale advective forc-  
423 ings, including positive temperature and moisture advection ahead of rainfall, and strong  
424 upper-level absolute vorticity advection during rainfall. The dynamic forcings ( $Adv_\zeta$  and  
425  $Adv_T$ ) induce a strong ascent that encourages local convection, while the moisture advec-  
426 tion premoistens the local convective environment, leading to stronger convection later. The  
427 temperature and moisture advection in ECN are significantly stronger than those in the  
428 SUS.

429 (2) There are regional differences in background circulations and synoptic perturbations  
430 associated with EPEs in ECN and the SUS. In ECN, the background absolute vorticity  
431 advection, warm advection, and moisture advection form the quasi-steady Mei-Yu front,  
432 which provides favorable conditions for synoptic perturbations to cause heavy rainfall. By  
433 contrast, in the SUS, there is only dynamically forced background ascent from absolute  
434 vorticity advection; the warm advection and moist advection are very weak. In the synoptic  
435 scale, the EPEs in ECN are associated with a short-wavelength wave train, while EPEs are  
436 triggered by large-scale PV intrusion in the SUS.

437 (3) Although the dynamically forced vertical motions in the two regions have similar  
438 amplitudes, the diabatic heating feedback in ECN is much stronger than that in the SUS.  
439 Qualitative analyses suggest that this outcome may due to the stronger modification of  
440 moisture advection, convective environments with more humidity, and a stronger coupling  
441 between convection and large-scale dynamics due to the shorter wavelength of the synoptic  
442 disturbances in ECN compared to those in the SUS.

443 This paper is mainly a diagnostic study with observational data. To quantitatively  
444 untangle the effects of background circulation and synoptic perturbations on the regional  
445 features of EPEs in ECN and the SUS, further studies are required with additional numerical  
446 simulations (e.g., *Nie et al.* 2016), such as a set of experiments with the same background  
447 large-scale or synoptic forcings. It is also worthwhile to examine the interannual variations

448 among the extreme events. It has been known that interannual variability patterns, such as  
449 the El Niño-Southern Oscillation, have significant influence on regional extreme precipitation  
450 (e.g., *Dayan et al.* 2015; *Whan and Zwiers* 2017). The analysis method used in this paper  
451 may fill the gap between remote teleconnections and local precipitation extremes. Over the  
452 long term, the responses of precipitation extremes to global warming will have dramatic  
453 regional variations (*Alexander et al.* 2006); the GCM results suggest that the increases in  
454 precipitation extremes in ECN will be greater than similar increases in the SUS (*Kharin*  
455 *et al.* 2007; *Pfahl et al.* 2017). One may use the QG $\omega$  equation to better understand the  
456 regional responses of extreme precipitation to climate change in extratropical regions.

457 *Acknowledgments.*

458 Acknowledgments

## REFERENCES

- 461 Alexander, L. V. , et al., 2006: Global observed changes in daily climate extremes of tem-  
462 perature and precipitation. *J Geophys Res* 111:D05109.
- 463 Cavalcanti, I. F. A., 2012: Cavalcanti. arge scale and synoptic features associated with  
464 extreme precipitation over South America: A review and case studies for the first decade  
465 of the 21st century, 118. 27-40.
- 466 Clough, S. A., C. S. A. Davitt, and A. J. Thorpe, 1996: Attribution concepts applied to the  
467 omega equation. *Quart. J. Roy. Me- teor. Soc.*, 122, 1943–1962.
- 468 Chen, Y., and P. Zhai, 2014: Precursor Circulation Features for Persistent Extreme Precip-  
469 itation in Central-Eastern China. *Weather and Forecasting*, 29, 226–240.
- 470 Chiang, J. C. H., L. M. Swenson, and W. Kong, 2017: Role of seasonal transitions and the  
471 westerlies in the interannual variability of the East Asian summer monsoon precipitation,  
472 *Geophysical Research Letters*, 44, 3788–3795.
- 473 Dayan, U., K. Nissen, and U. Ulbrich, 2015: Review Article: Atmospheric conditions in-  
474 ducing extreme precipitation over the eastern and western Mediterranean, *Nat. Hazards*  
475 *Earth Syst. Sci.*, 15, 25252544.
- 476 Dee, D. P. and coauthors, 2011: The era-interim reanalysis: configu- ration and performance  
477 of the data assimilation system, *Quarterly Journal of the Royal Meteorological Society*,  
478 137, 553–597.
- 479 Derbyshire, S. H., I. Beau, P. Bechtold, J. Y. Grandpeix, J. M. Piriou, J. L. Redelsperger,  
480 and P. M. M. Soares, 2004: Sensitivity of moist convection to environmental humidity,  
481 *Quart. J. Roy. Meteor. Soc.*, 130, 3055–3079.

482 Funatsu, B. M., and D. W. Waugh, 2008: Connections between Potential Vorticity Intrusions  
483 and Convection in the Eastern Tropical Pacific, *Journal of the Atmospheric Sciences*, 65,  
484 987–1002.

485 Funk, T. W., 1991: Forecasting techniques utilized by the Forecasting Branch of the National  
486 Meteorological Center during a major convective rainfall event. *Wea. Forecasting*, 6, 548–  
487 564.

488 Gu, W., L. Wang, Z. Hu, K. Hu, and Y. Li, 2018: Interannual Variations of the First Rainy  
489 Season Precipitation over South China, *Journal of Climate*, 31, 623–640.

490 Holton, J. 2004: *An introduction to dynamic meteorology*, Forth edition, Elsevier Academic  
491 Press, P164–168.

492 Houze, R. A., Jr., K. L. Rasmussen, S. Medina, S. R. Brodzik, and U. Romatschke, 2011:  
493 Anomalous atmospheric events leading to the summer 2010 floods in Pakistan, *Bull. Am.*  
494 *Meteorol. Soc.*, 92, 291–298.

495 Kharin, V. V., F. W. Zwiers, X. Zhang, G. C. Hegerl, 2007: Changes in temperature and  
496 precipitation extremes in the ipcc ensemble of global coupled model simulations. *Journal*  
497 *of Climate*, 20, 1419–1444.

498 Konrad, C. E., and V. Meentemeyer, 1994: Lower tropospheric warm air advection patterns  
499 associated with heavy rainfall over the Appalachian region. *Prof. Geog.*, 46, 143–155.

500 Konrad, C. E., 1997: Synoptic-Scale Features Associated with Warm Season Heavy Rainfall  
501 over the Interior Southeastern United States, *Wea. Forecasting*, 12, 557-571.

502 Lareau, N. P., and J. D. Horel, 2011: The Climatology of Synoptic-Scale Ascent over Western  
503 North America: A Perspective on Storm Tracks, *Mon. Weather Rev.*, 140, 1761–1778.

504 Lau, W. K., and K.-M. Kim, 2012: The 2010 Pakistan flood and Russian heat wave: Tele-  
505 connection of hydrometeorological extremes. *J. Hydrometeor.*, 13, 392–403.

506 Luo, Y., H. Wang, R. Zhang, W. Qian, and Z. Luo, 2013: Comparison of Rainfall Charac-  
507 teristics and Convective Properties of Monsoon Precipitation Systems over South China  
508 and the Yangtze and Huai River Basin. *Journal of Climate*, 26, 110–132.

509 Ma, K., and L. F. Bosart, 1990: A synoptic overview of a heavy rain event in southern  
510 China. *Wea. Forecasting*, 5, 89–112.

511 Maddox, R. A., C. F. Chappell, and L. R. Hoxit, 1979: Synoptic and meso scale aspects of  
512 flash flood events. *Bull. Amer. Meteor. Soc.*, 60, 115–123.

513 Maddox, R. A., F. Canova, and L. R. Hoxit, 1980: Meteorological characteristics of flash  
514 flood events over the western United States. *Mon. Wea. Rev.*, 108, 1866–1877.

515 Martius, O., C. Schwierz, and H. Davies, 2008: Far-upstream precursors of heavy precipita-  
516 tion events on the Alpine south-side. *Quart. J. Roy. Meteor. Soc.*, 134, 417–428.

517 Martius, O. and coauthors, 2013: The role of upper-level dynamics and surface processes for  
518 the Pakistan flood of July 2010, *Quarterly Journal of the Royal Meteorological Society*,  
519 139, 1780–1797.

520 Massacand, A. C., H. Wernli, H. C. Davies, 1998: Heavy precipitation on the Alpine south-  
521 side: An upper-level precursor. *Geophys. Res. Lett.* 25, 1435–1438.

522 Mo, K.C., and W. Higgins, 1998: The Pacific-South American modes and tropical convection  
523 during the Southern Hemisphere winter. *Mon. Weather Rev.* 126, 1581–1596.

524 Nie, J., W. R. Boos, and Z. Kuang, 2010: Observational Evaluation of a Convective Quasi-  
525 Equilibrium View of Monsoons, *Journal of Climate*, 23, 4416–4428.

526 Nie, J. and A. H. Sobel, 2016: Modeling the interaction between quasigeostrophic vertical  
527 motion and convection in a single column, *Journal of the Atmospheric Sciences*, 73, 1101–  
528 1117.

529 Nie, J., D. Shaevitz, and A. H. Sobel, 2016: Forcings and Feedback in the 2010 Pakistan  
530 Flood: Modeling Extreme Precipitation with Interactive Large-Scale Ascent, *Journal of*  
531 *Advances in Modeling Earth Systems*, 8, 1055–1072.

532 Nie, J., A. H. Sobel, D. Shaevitz, and S. Wang, 2018: Dynamic Amplification of Extreme  
533 Precipitation Sensitivity, *Proc. Natl. Acad. Sci.*, 115, 9467–9472.

534 OGorman, P. A., T. Schneider, 2009: The physical basis for increases in precipitation ex-  
535 tremes in simulations of 21st-century climate change. *Proc. Natl. Acad. Sci.* 106:14773–  
536 14777.

537 Peixoto, J. P., and A. H. Oort, 1992, *Physics of Climate*, First edition, American Institute  
538 of Physics, P167, P280.

539 Pfahl, S., P. A. OGorman, E. M. Fischer, 2017: Understanding the regional pattern of  
540 projected future changes in extreme precipitation, *Nat Clim Change*, 7,423-428.

541 Rodwell, M. J. and B. J. Hoskins, 2001: Subtropical Anticyclones and Summer Monsoons,  
542 *Journal of Climate*, 14, 3192–3211.

543 Sampe, T. and S.-P. Xie, 2010: Large-Scale Dynamics of the Meiyu-Baiu Rainband: Envi-  
544 ronmental Forcing by the Westerly Jet, *Journal of Climate*, 23, 113–134.

545 Shaevitz, D. A., 2016: Extreme weather: subtropical floods and tropical cyclones, PhD diss.,  
546 Columbia University, New York.

547 Shiu, C. J., S. C. Liu, C. Fu, A. Dai, Y. Sun, 2012: How much do precipitation extremes  
548 change in a warming climate? *Geophysical Research Letters*, 39.

549 Stone, H. L.,1968: Iterative solution of implicit approximations of multidimensional partial  
550 differential equations., *SIAM Journal of Numerical Analysis*, 5, 530–558.

551 Sun, J. and F. Zhang, 2017: Daily extreme precipitation and trends over China, *SCIENCE*  
552 *CHINA Earth Sciences*, 60, 2190–2203.

553 Tandon, N. F., X. Zhang, A. H. Sobel, 2018. Understanding the dynamics of future changes  
554 in extreme precipitation intensity. *Geophysical Research Letters*, 45, 2870–2878.

555 Tandon, N. F., J. Nie, and X. Zhang, 2018: Strong Influence of Eddy Length on  
556 Boreal Summertime Extreme Precipitation Projections, *Geophysical Research Letters*,  
557 doi.org/10.1029/2018GL079327.

558 Uccellini, L. W., and P. J. Kocin, 1987: The interaction of jet streak circulations during  
559 heavy snow events along the East Coast of the United States. *Wea. Forecasting*, 2, 289–  
560 308.

561 Wan, B., Z. Gao, F. Chen, and C. Lu, 2017: Impact of Tibetan Plateau Surface Heating on  
562 Persistent Extreme Precipitation Events in Southeastern China, *Monthly Weather Review*,  
563 145, 3485–3505.

564 Wang, W.-C., W. Gong, and H. Wei, 2000: A regional model simulation of the 1991  
565 severe precipitation event over the Yangtze Huai River valley. Part I: Precipitation and  
566 circulation statistics. *J. Climate*, 13, 74–92.

567 Waugh, D. W., and L. M. Polvani, 2000: Climatology of intrusions into the tropical upper  
568 troposphere. *Geophys. Res. Lett.* 27, 3857–3860.

569 Whan, K., and F. Zwiers, 2017: The impact of ENSO and the NAO on extreme winter  
570 precipitation in North America in observations and regional climate models, 48, 1401–  
571 1411.

572 van der Wiel, K, S. B. Kapnick, G. A. Vecchi, W. F. Cooke, T. L. Delworth, L. Jia, H.  
573 Murakami, S. Underwood, F. Zeng, 2016: The resolution dependence of contiguous US  
574 precipitation extremes in response to CO2 forcing. *Journal of Climate*, 29, 7991–8012.

575 Wirth, V., and J. Eichhorn, 2014: Long-lived Rossby wave trains as precursors to strong  
576 winter cyclones over Europe. *Q. J.R. Meteorol. Soc.* 140: 729–737.

- 577 Yihui, D., and J. C. Chan, 2005: The East Asian summer monsoon: An overview. Meteor.  
578 Atmos. Phys., 89, 117–142.
- 579 Zhou, T.-J., and R.-C. Yu, 2005: Atmospheric water vapor transport associated with  
580 typical anomalous summer rainfall patterns in China. J. Geophys. Res., 110, D08104,  
581 doi:10.1029/2004JD005413.

582 **List of Tables**

583 1 Precipitation (units in *mm/day*) in reanalysis and approximated by  $\omega$ . The  
584 last column is for the diabatic heating feedback parameter  $\alpha$ . 26

TABLE 1. Precipitation (units in  $mm/day$ ) in reanalysis and approximated by  $\omega$ . The last column is for the diabatic heating feedback parameter  $\alpha$ .

	$P(reanalysis)$	$P(scaling)$	$P_D$	$P_Q$	$P_{agg}$	$\alpha$
ECN	17.5	17.5	5.0	10.3	2.2	2.1
SUS	11.7	10.2	4.9	5.2	0.1	1.1

## 585 List of Figures

- 586 1 The time evolution of the regional averaged advective forcings associated with  
587 the EPEs in ECN (left column) and the SUS (right column). From top to  
588 bottom, the panels are  $Adv_\zeta$ ,  $Adv_T$ , and  $Adv_q$ , respectively. The x-axis is  
589 time with day 0 marking the day with peak precipitation. The y-axis is the  
590 pressure level. 29
- 591 2 The decomposition of advective terms for the ECN regions. From top to  
592 bottom, the panels are  $Adv_\zeta$ ,  $Adv_T$ , and  $Adv_q$ . From left to right, the columns  
593 are the RHS-1, the sum of RHS-2 and RHS-3, and the RHS-4 term of Eq. 3. 30
- 594 3 Same as in Fig. 2, except the results are for the SUS region. 31
- 595 4 The time evolution of  $\omega$  components. The left column is for ECN and the  
596 right column is for the SUS. From top to bottom, the panels are  $\omega_\zeta$ ,  $\omega_T$ ,  $\omega_Q$ ,  
597 and total  $\omega$ , respectively. Note that the colorbars of each row are different.  
598 The x-axis is time, with day 0 marking the day with peak precipitation. The  
599 y-axis is the pressure level. 32
- 600 5 The background geopotential (colormap with units of  $m^2/s^2$ ) and horizontal  
601 winds (vectors with units of  $m/s$ ) at 850  $hPa$  (the first row), 500  $hPa$  (the  
602 second row), and 200  $hPa$  (the third row). The last row shows the background  
603 precipitable water (colormap with units of  $mm/m^2$ ) superimposed on 850  $hPa$   
604 background winds. The left column is for the ECN region, while the right  
605 column is for the SUS region. Grids with a surface pressure larger than the  
606 pressure levels are masked. 33
- 607 6 Same as in Fig. 5, except the results are the differences between the back-  
608 ground states and the summer season means. 34
- 609 7 The synoptic-scale geopotential (color contours) and horizontal winds (vec-  
610 tors) at 200  $hPa$ . From left to right shows day -1, day 0 and day +1. The top  
611 panels are for the ECN region, and the lower panels are for the SUS region. 35

612	8	The horizontal distribution of the $\omega$ (the top row), the sum of $\omega_\zeta$ and $\omega_T$ (the middle row), and $\omega_Q$ (the bottom row) at 500 <i>hPa</i> on day 0. The white dashed contour lines denote a heavy-rainfall area (day 0 precipitation greater than 20 <i>mm/day</i> in ECN and greater than 12 <i>mm/day</i> in the SUS.	36
613			
614			
615			
616	9	The vertical profile of $\omega$ and its components averaged over the two regions on day 0.	37
617			
618	10	The regional-box averaged $T$ (a), $q$ (b), $\sigma$ (c), and relative humidity (d) on day 0.	38
619			
620	11	Schematic of the factors associated with EPEs in ECN (a) and the SUS (b). The factors in black indicate slow-varying backgrounds, and the factors in color (positive in red and negative blue) indicate synoptic-scale perturbations. Arrows denote winds, and the associated advection that plays a role in EPEs are also marked. In ECN, the important background factors are the southwest-extended Pacific subtropical high, the South Asia high, and the south-shifted westerly jet. In the synoptic scale, a short-wavelength wave train in the upper troposphere is associated with a westward-tilted low-pressure center below in addition to strong and deep convection. In the SUS, the important background factors are the Atlantic subtropical high in the lower troposphere, the tropical high in the middle and upper troposphere, and the westerly jet. In the upper troposphere, a planetary-scale wave train provides strong PV intrusion from higher latitudes. The PV intrusion energizes the development of the cyclone and strong convection below. The size of the cloud symbol in ECN is larger than that in the SUS, which indicates that there is stronger diabatic heating feedback and precipitation there.	39
621			
622			
623			
624			
625			
626			
627			
628			
629			
630			
631			
632			
633			
634			
635			

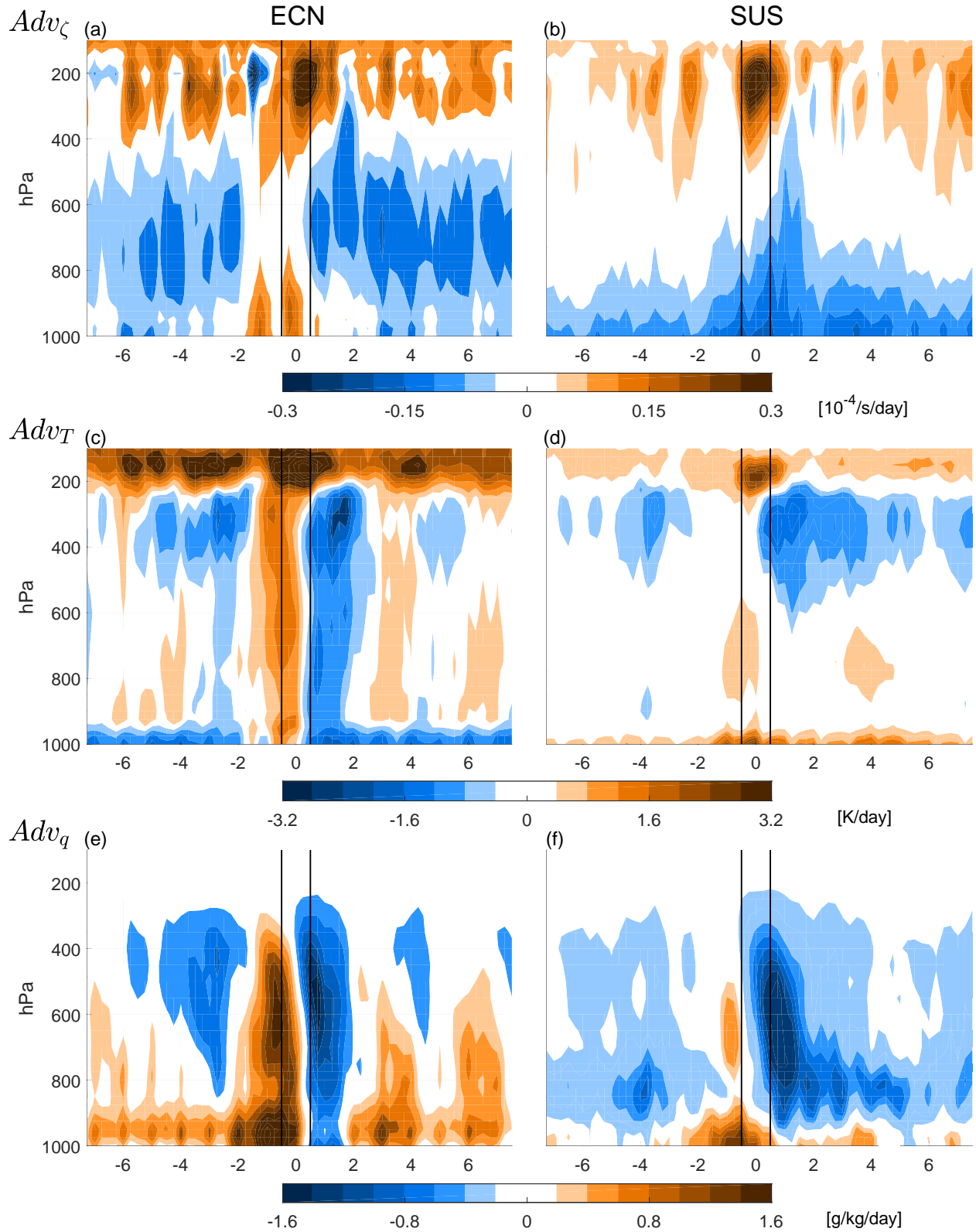


FIG. 1. The time evolution of the regional averaged advective forcings associated with the EPEs in ECN (left column) and the SUS (right column). From top to bottom, the panels are  $Adv_\zeta$ ,  $Adv_T$ , and  $Adv_q$ , respectively. The x-axis is time with day 0 marking the day with peak precipitation. The y-axis is the pressure level.

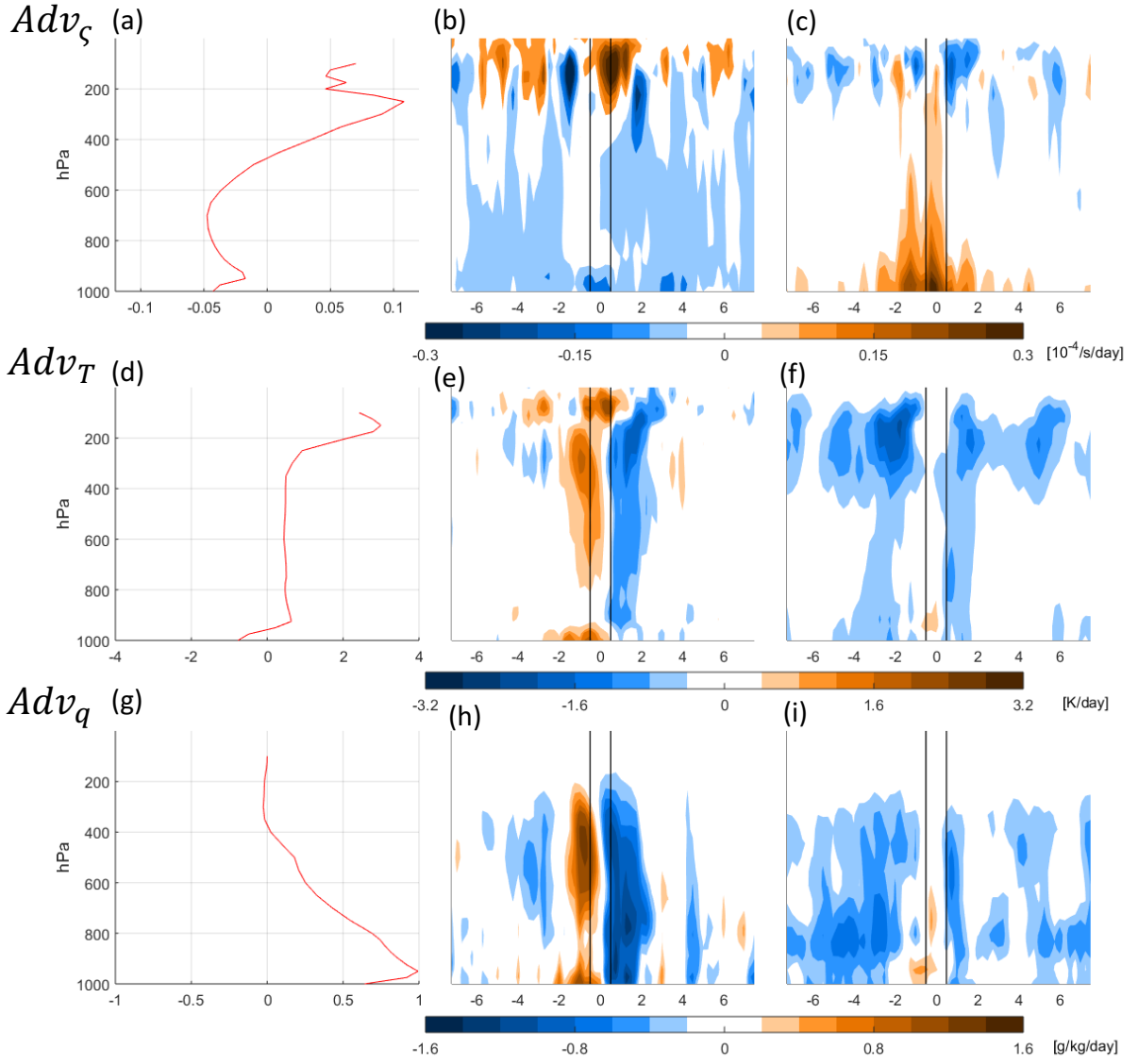


FIG. 2. The decomposition of advective terms for the ECN regions. From top to bottom, the panels are  $Adv_\zeta$ ,  $Adv_T$ , and  $Adv_q$ . From left to right, the columns are the RHS-1, the sum of RHS-2 and RHS-3, and the RHS-4 term of Eq. 3.

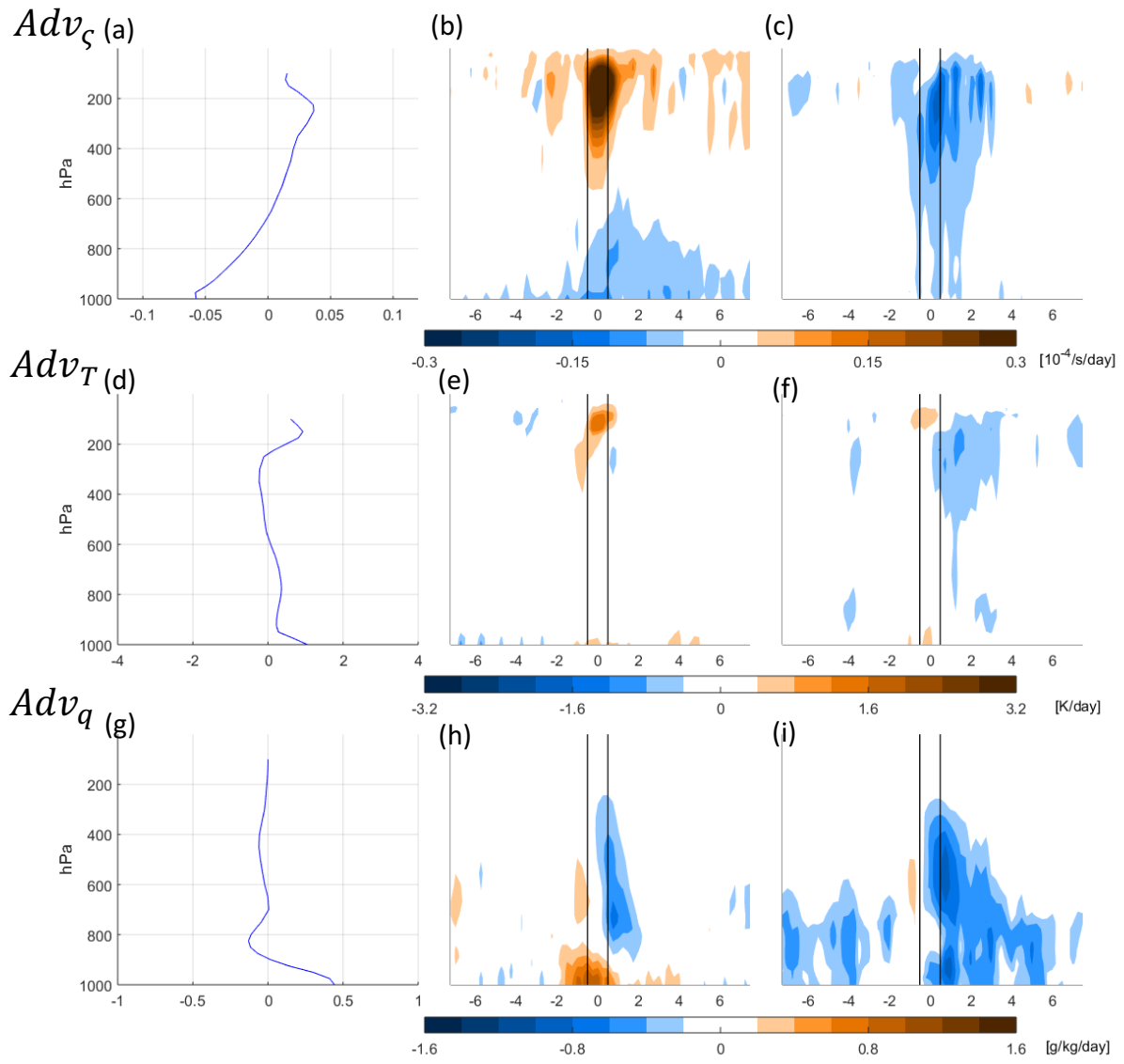


FIG. 3. Same as in Fig. 2, except the results are for the SUS region.

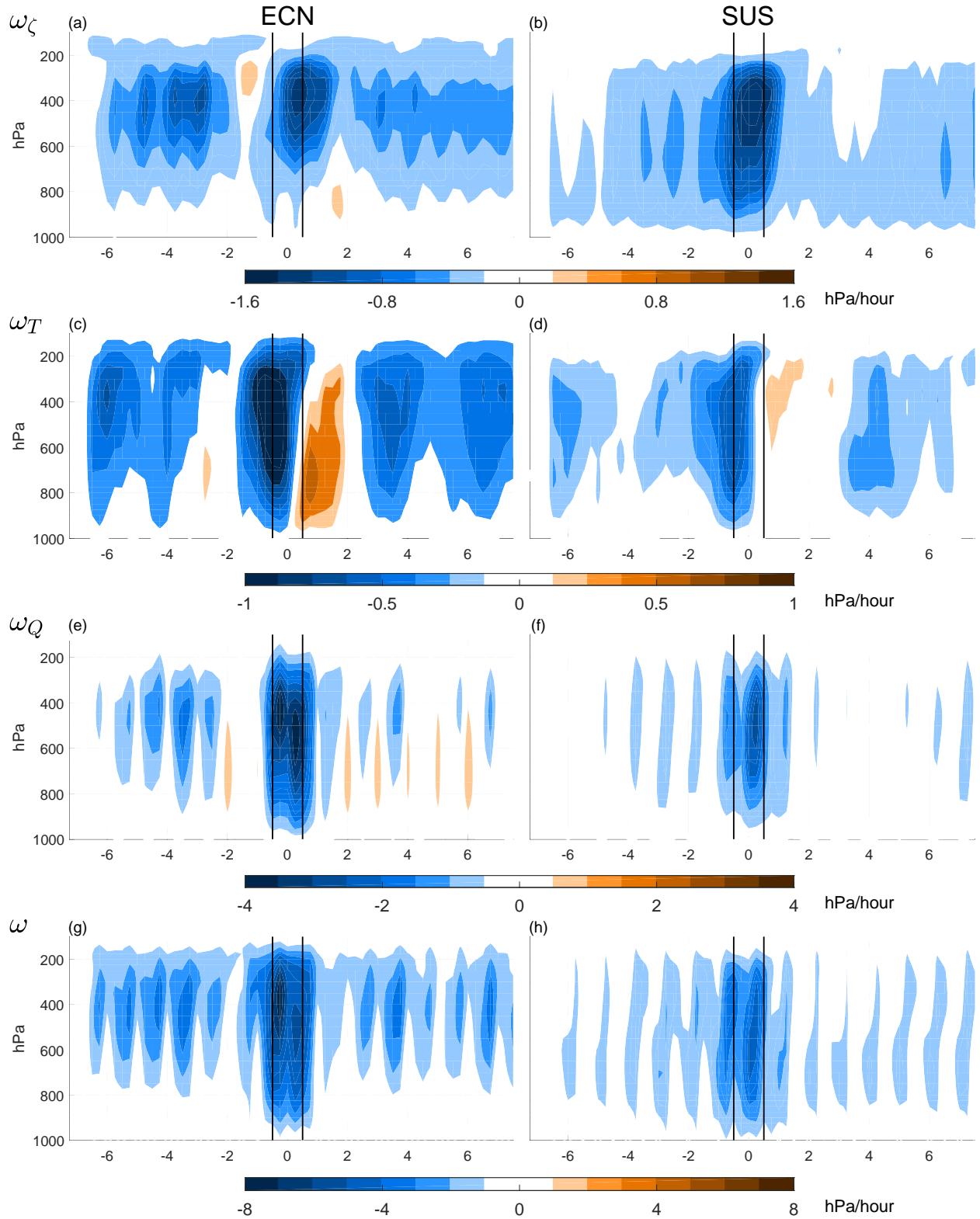


FIG. 4. The time evolution of  $\omega$  components. The left column is for ECN and the right column is for the SUS. From top to bottom, the panels are  $\omega_\zeta$ ,  $\omega_T$ ,  $\omega_Q$ , and total  $\omega$ , respectively. Note that the colorbars of each row are different. The x-axis is time, with day 0 marking the day with peak precipitation. The y-axis is the pressure level.

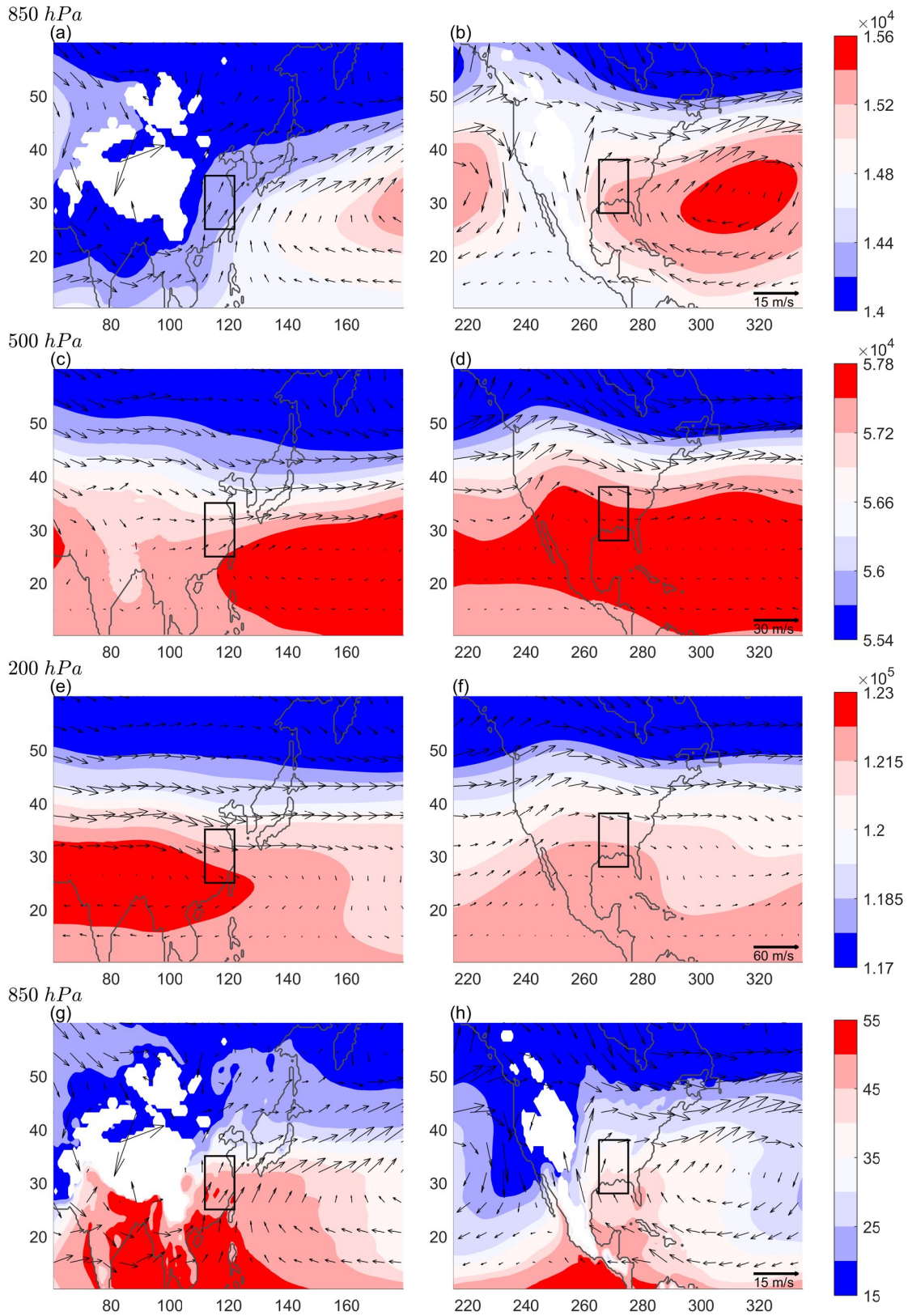


FIG. 5. The background geopotential (colormap with units of  $m^2/s^2$ ) and horizontal winds (vectors with units of  $m/s$ ) at 850  $hPa$  (the first row), 500  $hPa$  (the second row), and 200  $hPa$  (the third row). The last row shows the background precipitable water (colormap with units of  $mm/m^2$ ) superimposed on 850  $hPa$  background winds. The left column is for the ECN region, while the right column is for the SUS region. Grids with a surface pressure larger than the pressure levels are masked.

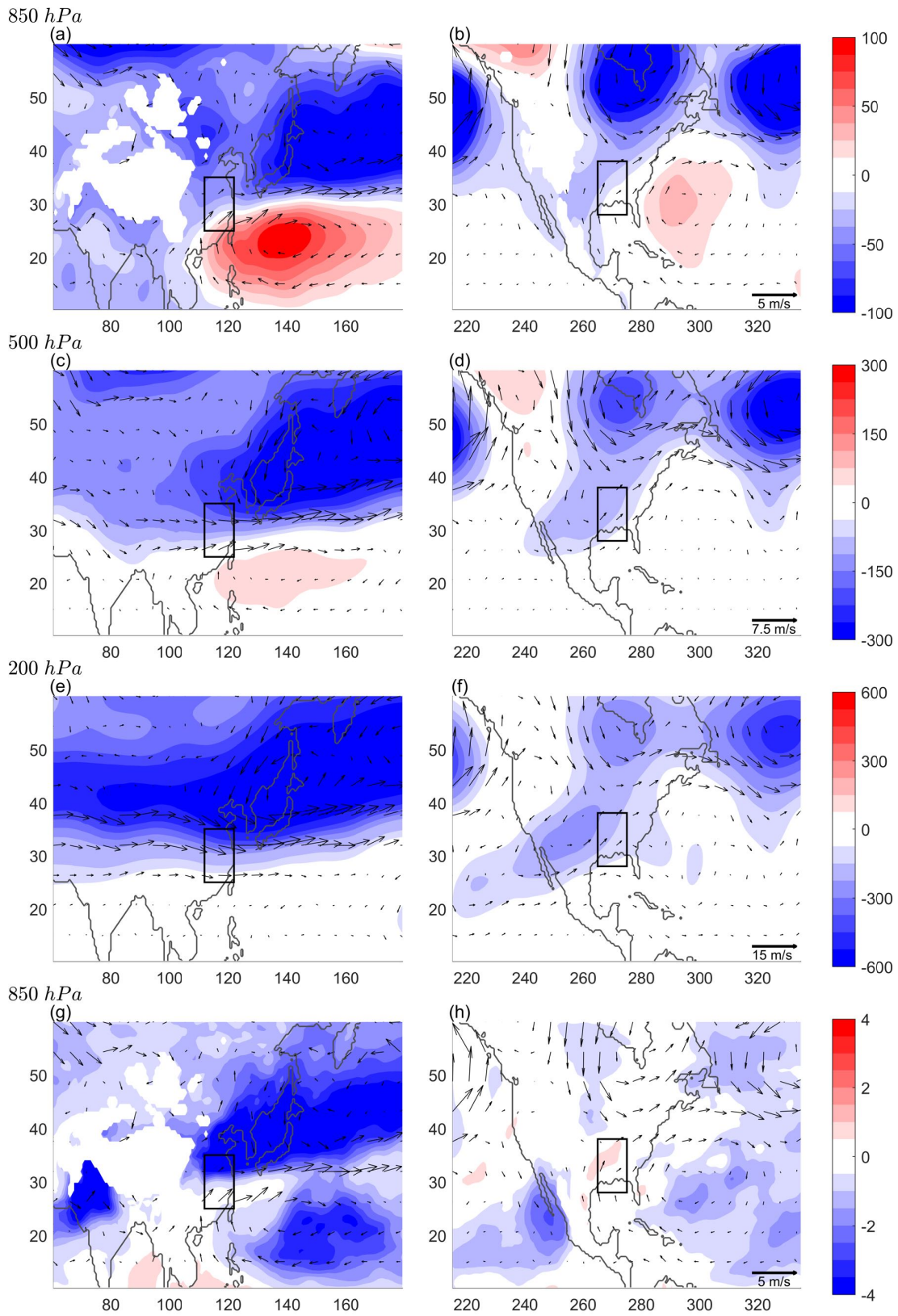


FIG. 6. Same as in Fig. 5, except the results are the differences between the background states and the summer season means.

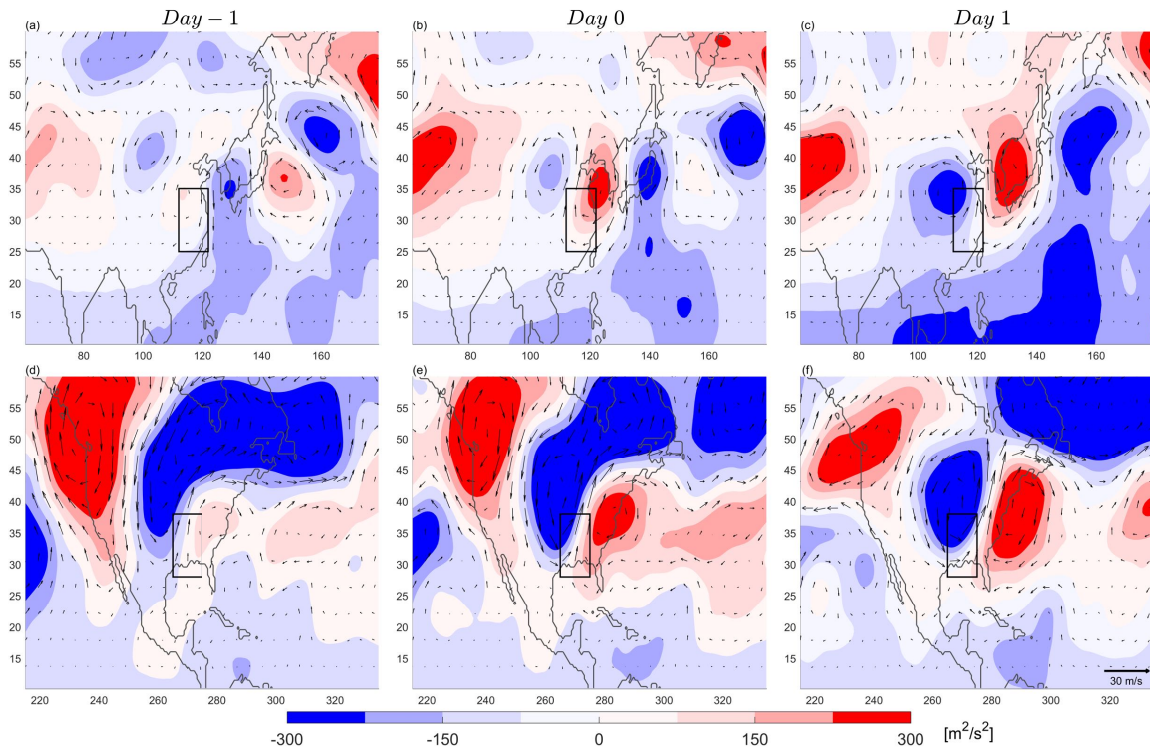


FIG. 7. The synoptic-scale geopotential (color contours) and horizontal winds (vectors) at 200  $hPa$ . From left to right shows day -1, day 0 and day +1. The top panels are for the ECN region, and the lower panels are for the SUS region.

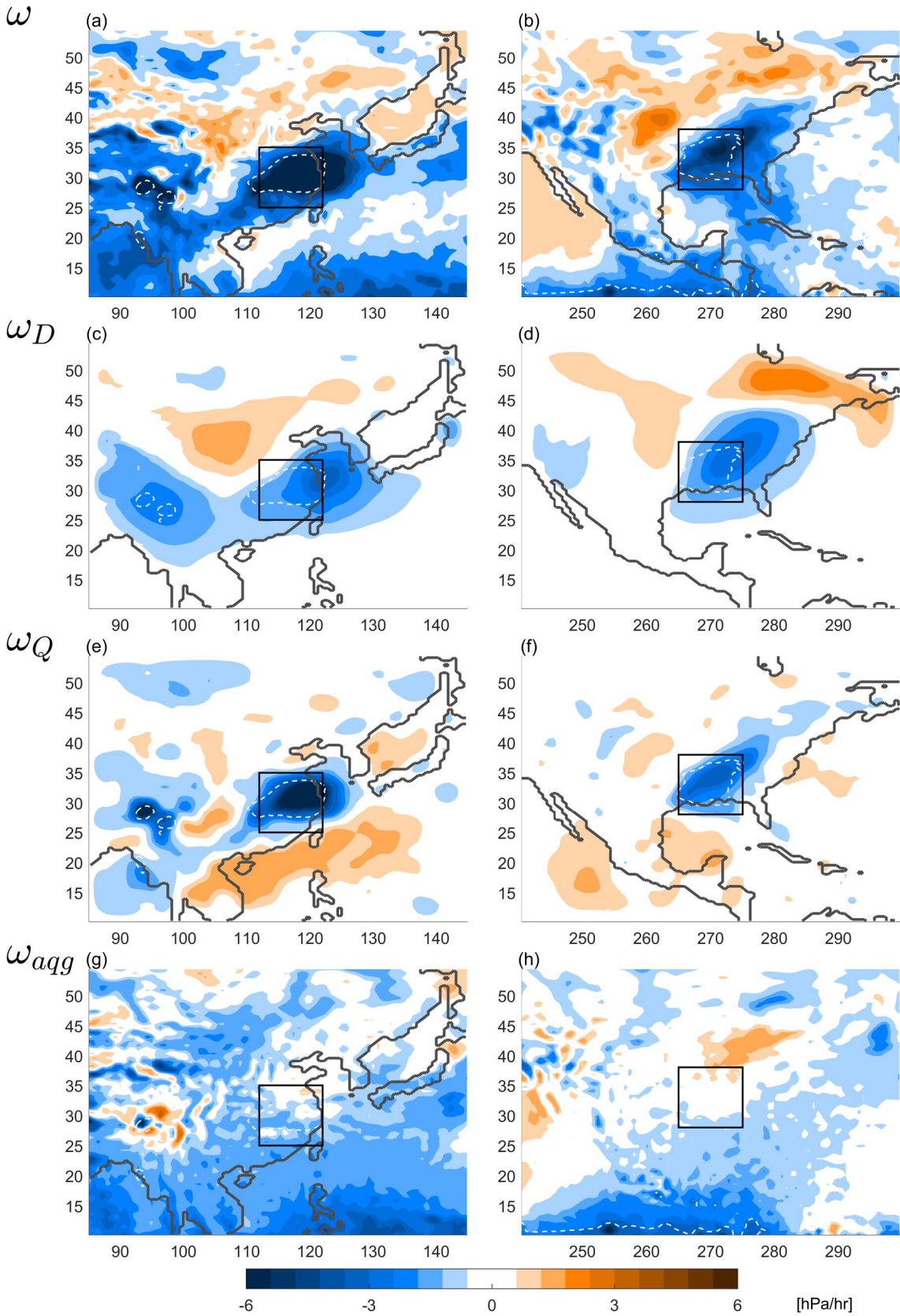


FIG. 8. The horizontal distribution of the  $\omega$  (the top row), the sum of  $\omega_\zeta$  and  $\omega_T$  (the middle row), and  $\omega_Q$  (the bottom row) at 500 hPa on day 0. The white dashed contour lines denote a heavy-rainfall area (day 0 precipitation greater than 20 mm/day in ECN and greater than 12 mm/day in the SUS).

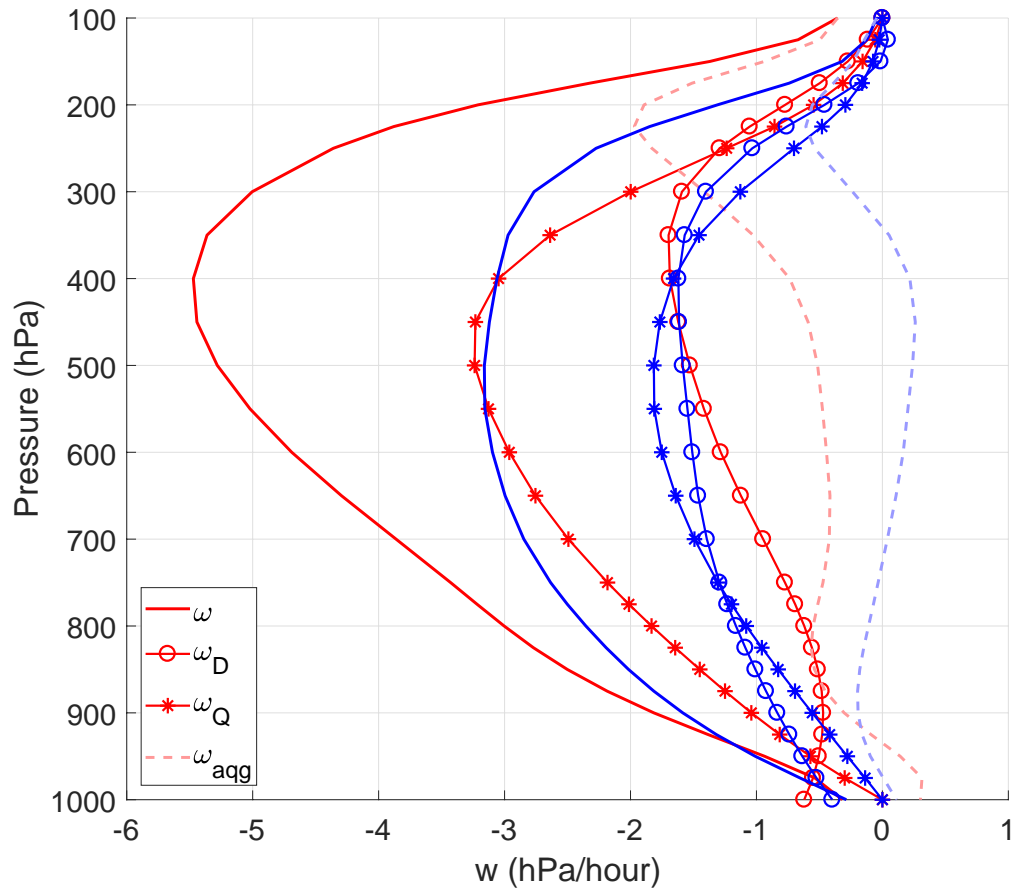


FIG. 9. The vertical profile of  $\omega$  and its components averaged over the two regions on day 0.

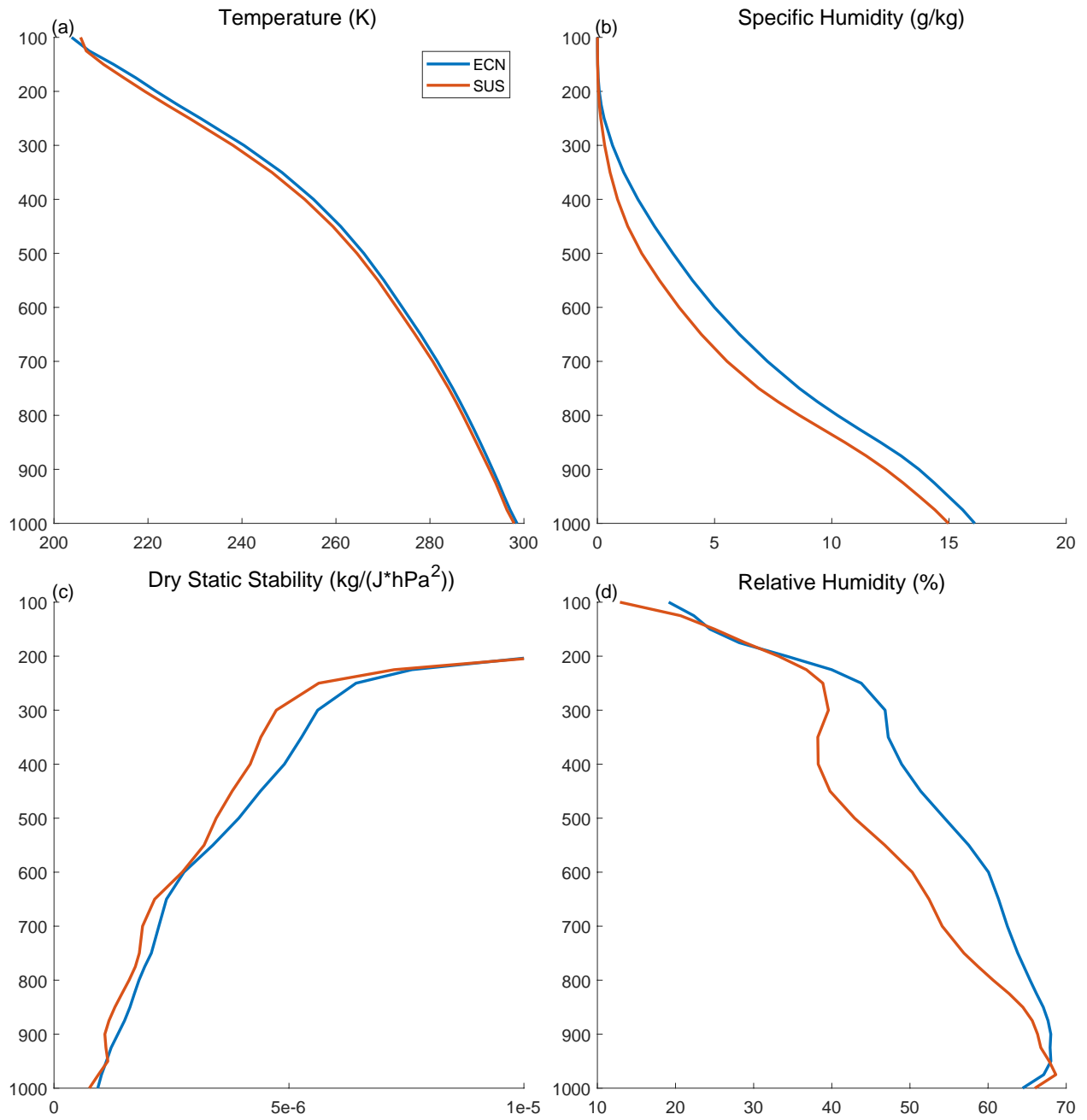


FIG. 10. The regional-box averaged  $T$  (a),  $q$  (b),  $\sigma$  (c), and relative humidity (d) on day 0.

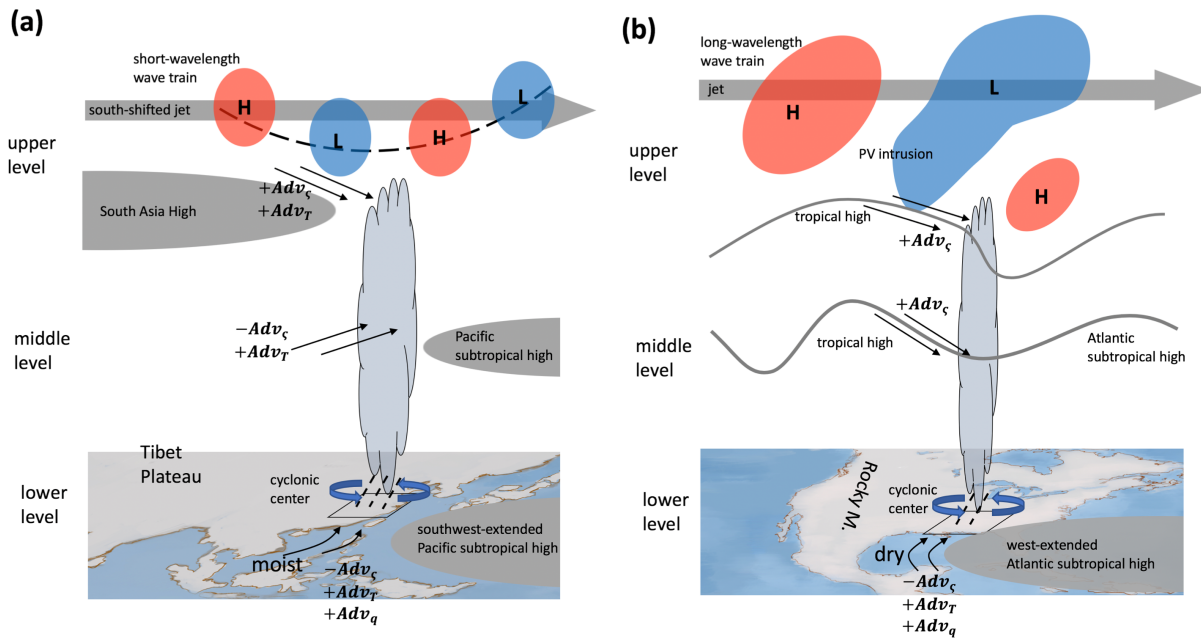


FIG. 11. Schematic of the factors associated with EPEs in ECN (a) and the SUS (b). The factors in black indicate slow-varying backgrounds, and the factors in color (positive in red and negative blue) indicate synoptic-scale perturbations. Arrows denote winds, and the associated advection that plays a role in EPEs are also marked. In ECN, the important background factors are the southwest-extended Pacific subtropical high, the South Asia high, and the south-shifted westerly jet. In the synoptic scale, a short-wavelength wave train in the upper troposphere is associated with a westward-tilted low-pressure center below in addition to strong and deep convection. In the SUS, the important background factors are the Atlantic subtropical high in the lower troposphere, the tropical high in the middle and upper troposphere, and the westerly jet. In the upper troposphere, a planetary-scale wave train provides strong PV intrusion from higher latitudes. The PV intrusion energizes the development of the cyclone and strong convection below. The size of the cloud symbol in ECN is larger than that in the SUS, which indicates that there is stronger diabatic heating feedback and precipitation there.